Fluorescent Microporous Polyimides based on Perylene and Triazine for Highly CO_2-Selective Carbon Materials

Yaozu Liao,[a] Jens Weber[b] and Charl F.J. Faul[a*]

[a] School of Chemistry, University of Bristol, Bristol, England BS8 1TS, UK.

[b] Hochschule Zittau/Görlitz (University of Applied Science), Department of Chemistry, Theodor-Körner-Allee 16, D-02763 Zittau, GERMANY

*Corresponding author: charl.faul@bristol.ac.uk

Abstract

Carbon dioxide (CO_2) capture from point sources like coal-fired power plants is a potential solution for stabilizing atmospheric CO_2 content to avoid global warming. Sorbents with high and reversible CO_2 uptake, high CO_2 selectivity, good chemical and thermal stability and low cost are desired for the separation of CO_2 from N_2 in flue or natural gas. We report here, for the first time, on the synthesis of new microporous polyimide (PI) networks from the condensation of perylene-3,4,9,10-tetracarboxylic dianhydride (PTCDA) and 1,3,5-triazine-2,4,6-triamine (melamine) using a Lewis acid catalyst zinc acetate/imidazole complex. These PI network materials, prepared in the absence and presence of dimethyl sulfoxide (DMSO) as weak solvent template, exhibit strong fluorescence. Nitrogen-containing carbons can be accessed from our PI networks *via* a simple thermal pyrolysis route. The successful construction of new microporous PI networks and derived N-containing carbons is shown here to provide promising CO_2 sorbents with high uptake capacities (15 wt%) combined with exceptional selectivities over N_2 (240), whilst their fluorescent properties can be exploited for simple sensing.

Introduction

Carbon dioxide (CO_2) capture from point sources like coal-fired power plants is a potential solution for stabilizing atmospheric CO_2 content to avoid global warming.[1] Sorbents with high and reversible CO_2 uptake, high CO_2 selectivity, good chemical and thermal stability and low cost are desired for the separation of CO_2 from N_2 in flue or natural gas. It has recently been shown that porous organic polymers (POPs) are promising CO_2 sorbents because of their simple syntheses and high physicochemical stabilities, combined with high surface areas and unique porosities and low skeleton densities.[2] This field of research has witnessed the emergence of several new types of POPs including polymers of intrinsic microporosity (PIMs),[3] covalent organic frameworks (COFs),[4] covalent triazine-based frameworks (CTFs),[5] conjugated microporous polymers (CMPs)[6] and hyper-cross-linked polymers (HCPs).[7]

In order to maximize the CO_2 uptake capacity, a great deal of work, beside optimization of pore sizes, has focused on the introduction of polarizable sites through post-synthesis modification or introduction of nitrogen-rich and/or oxygen-rich building blocks to increase the CO_2–POP interaction energy *via* either dipole–quadrupole or hydrogen-bonding interactions, or both.[8-10] However, post-synthetic modification requires additional synthetic efforts, and makes this route less attractive (especially for large-scale application). This approach usually also leads to a decrease of surface areas and pore blocking. To avoid these obstacles, careful selection of functionalized building blocks as starting materials and the introduction of chemical heterogeneity in the polymerization protocol are feasible options.[6] Recent studies showed that the CO_2 uptake of several CMPs could be improved by substituting a phenyl node for a triazine unit, which also provides opportunities for further functionalization,[11] e.g., to efficiently immobilize platinum nanoparticles, activate and convert methane[12] and improve hydrogen generation.[13] Despite these advances, it is still highly desirable to improve the CO_2 storage capacity and selectivity through the development of new materials that require no post-synthetic modifications or processing.

Microporous polyimide (PI) networks[14] are attractive for energy storage applications because of their high mechanical strength, interesting redox behavior, good thermal stability and outstanding chemical resistance compared with other porous polymers. Selective CO_2 adsorption (over N_2 or CH_4) and good H_2 uptake has been reported recently for this class of POPs.[9,10,13,15-21] Microporous PI networks are usually synthesized in solution by condensation of polyamines and dianhydrides,

including pyromellitic dianhydride (PMDA), 3,3',4,4'-biphenyltetracarboxylic dianhydride (BPDA), naphthalene-1, 4, 5, 8-tetracarboxylicdianhydride (NTCD), and triptycene-based dianhydride (TPDA). These reactions are typically performed in high boiling point organic solvents such as *m*-cresol,[10,18,20] imidazole,[19] dimethyl sulfoxide (DMSO)[15] and isoquinoline.[15,20] Such solvents, especially DMSO, have been shown to interact with formed network structures, and serve as weak templates for the formation and control of porosity in CMPs.[22-24] Interestingly, a well-known and commercially available dianhydride, perylene-3,4,9,10-tetracarboxylic dianhydride (PTCDA), has rarely been used to make such promising PI networks,[18,19] probably due to its high rigidity and poor processability in non-aqueous solvents. In particular, no effort has – to the best of our knowledge – been devoted to combine the functionalities of PTCDA and triazine.

In this study, we report the synthesis of new microporous PI networks from the condensation of PTCDA and 1,3,5-triazine-2,4,6-triamine (melamine) using a Lewis acid catalyst zinc acetate/imidazole complex[25] (**Scheme 1**). These reactions are performed in both the absence and presence, at different concentrations, of DMSO, a good solvent for both starting compounds. Notably, both the perylene and triazine precursors used in this study have a planar structure, which is in contrast to the contorted structures of monomers used in most previously reported microporous PI networks. As perylene derivatives have interesting optical properties, we present initial data on the exploitation of these attractive materials as sensors. Finally, nitrogen-containing carbons can be accessed from our PI networks *via* a simple thermal pyrolysis route. The successful construction of new microporous PI networks and the derived N-containing carbons is shown here to provide promising CO_2 sorbents with high uptake capacities and selectivities.

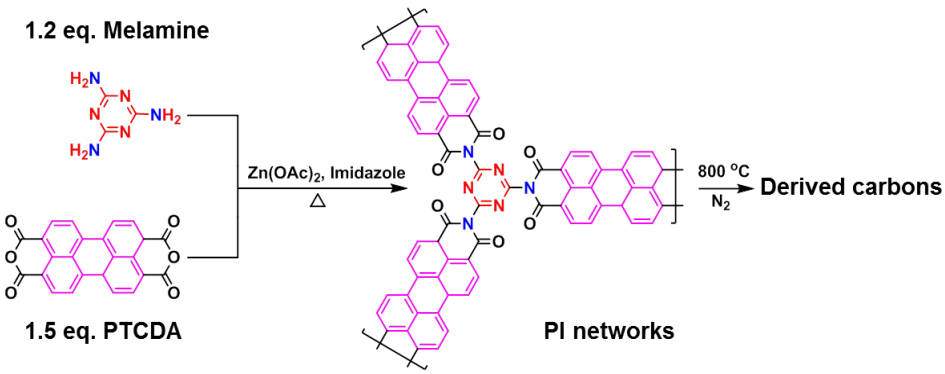

Scheme 1 Synthetic route to PI networks and derived nitrogen-doped carbons.

Results and Discussion

Synthesis, chemical structure and physical properties. PI networks were prepared in the absence (**PI-2**) and presence of DMSO at a fixed concentration ($c_{melamine}$ = 15 g L^{-1}, denoted as **PI-1**), thus exploring the influence of this co-solvent on the physicochemical properties of the obtained polymers. The zinc acetate/imidazole catalyst−solvent complex solubilized the PTCDA efficiently,[25] and afforded a homogenous reaction mixture with melamine to yield black insoluble microporous PIs in yields of 45-60% after 72 h (see Experimental, **Figure S1**).

Scanning electron microscopy (SEM) images revealed that the morphology of **PI-1** consists of uniformly condensed large particles of several micrometers in dimension and hundreds of nanometers thick (**Figure 1**), similar to the morphologies observed in PPV-, aza- and FeP-based CMPs.[26] In contrast, the morphology of **PI-2** comprised of irregular aggregates. Transmission electron microscope (TEM) images for both networks showed typical irregular structures as usually found for microporous polymer morphologies (**Figure S2**).

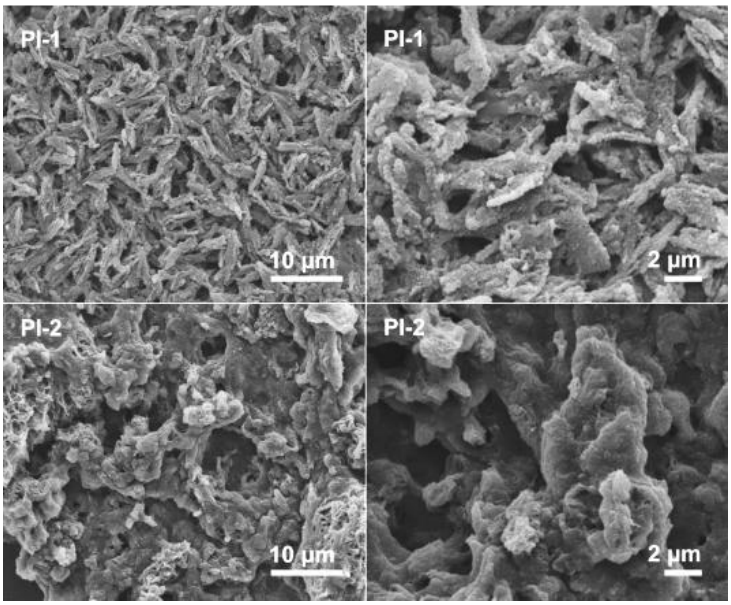

Figure 1 SEM images of **PI-1** and **PI-2** at (left) low and (right) high magnifications.

The PI networks exhibited good thermal stability with the onset of decomposition at ca. 400 ºC and char yields up to 45% at 1000 ºC in N_2 (**Figure S3**, as determined by thermogravimetric analysis, TGA). Small weight losses were observed at the initial stages due to solvent trapped inside the polymer networks. The high thermal stability of these PIs is ascribed to the covalent

linkages and high cross-linking density of the networks formed (in addition to the intrinsic thermal stability of the used perylene materials). Direct pyrolysis of **PI-1** in argon at 800 °C generated 68% char product. Fourier transform infrared (FT-IR) spectra of the char showed that the carbonyl and imide peaks became invisible (**Figure S4**), implying that a PI-based carbon material (**PI-1-C**) was successfully created. Elemental analyses, SEM (**Figure 2**) and TEM (**Figure 3** and **Figure S5**) results indicated that **PI-1-C** has a microporous structure with a nitrogen content of 3% (maximum 8% in theory). Selected area electron diffraction (SAED) analysis showed that **PI-1-C** is an amorphous carbon material (see **Figure S5**). Energy dispersive X-ray (EDX) spectra (**Figure S6**) and elemental analyses indicated that zinc and sulfur residues were present at very low concentrations (0.09 and 0.08%, respectively) in **PI-1-C.**

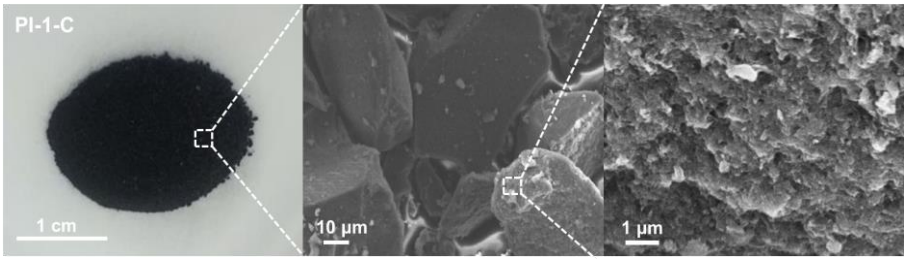

Figure 2 Carbon materials obtained *via* simple thermal pyrolysis of **PI-1** at 800 °C in argon.

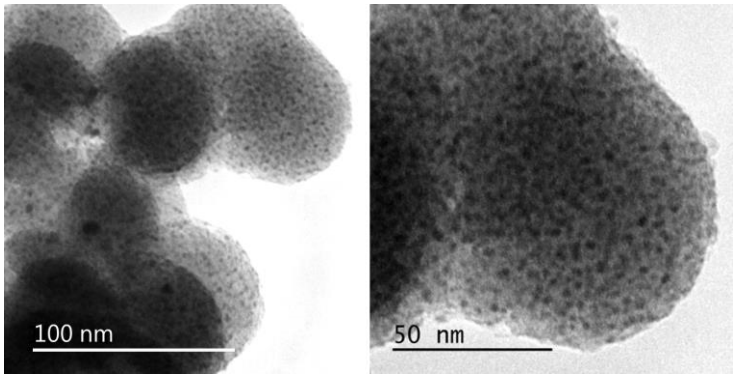

Figure 3 TEM images of **PI-1-C** at (left) low and (right) high magnifications.

PI network connectivity and the presence of derivatives of both building blocks were confirmed by solid-state ultraviolet visible near infrared (UV-Vis/NIR) and FT-IR spectroscopies. The UV-Vis absorption band edges of **PI-1** and **PI-2** are ~1340 and 1360 nm, corresponding to low band gap energies of 0.93 and 0.91 eV (**Figure 4**), respectively, which stand in noticeable contrast to the values observed in the respective monomers, melamine (320 nm, 3.88 eV) and PTCDA (670 nm, 1.85 eV), clearly indicating that products with new optoelectronic properties were formed. As

shown in **Figure 5**, the FT-IR spectra of **PI-1** and **PI-2** showed that the carbonyl stretch frequency shifted toward lower energy by approximately 70 cm^{-1} relative to PTCDA (ν_{imide}, 1685 *vs.* $\nu_{carboxylicdianhydride}$, 1755 cm^{-1}), indicating imide bond formation.[15,21] The free primary amine ($–NH_2$) stretch vibrations at 3468 and 3417 cm^{-1} were undetectable, suggesting complete conversion of the starting melamine primary amine groups. No strong signals of either the carboxyl (–COOH, 1740~1706 cm^{-1}) stretching vibrations or dianhydride (–COOOC–, 1300 cm^{-1}) bending vibrations were visible in the FT-IR spectra of the products. These results indicate that the imide ring closure worked well, apart from a few defects, which are always expected during the formation of highly cross-linked polymer networks.

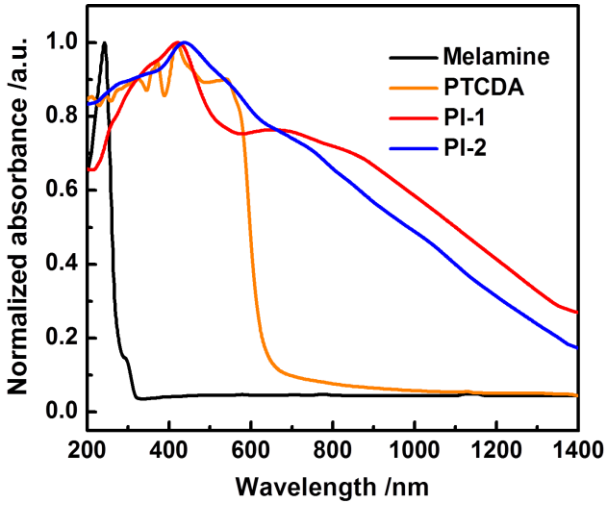

Figure 4 Solid-state UV-Vis/NIR spectra of melamine, PTCDA, **PI-1** and **PI-2**.

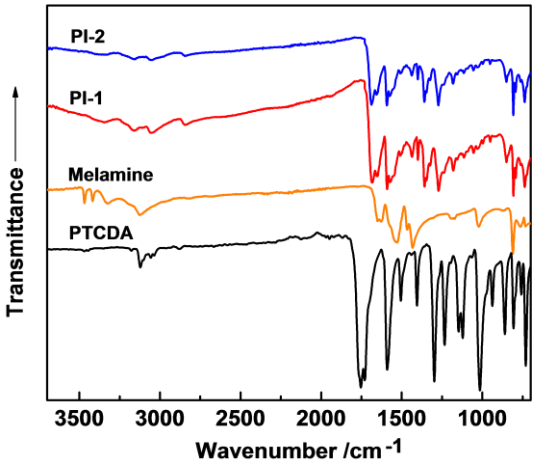

Figure 5 FT-IR spectra of PTCDA, melamine, **PI-1**, and **PI-2**.

Detailed analysis of the chemical structure of the PI networks was further performed by solid-state ^{13}C cross-polarization magic angle spinning (CP/MAS) NMR spectrometry. The ^{13}C CP/MAS

NMR spectrum of **PI-1** showed three resonances at 165, 161 and 128 ppm (**Figure S7**). The first two very weak resonances were assigned to the carbon atoms present in the triazine ring of the melamine core[15,27] and the carbonyl group of the imide,[15,21] respectively, whereas the multiple signals centered at 128 ppm originated from the CH aromatic carbons of the perylene units. Resonances at 195 and 60 ppm are ascribed to spinning sidebands. The results show, in accordance with the results from the UV-Vis/NIR and FT-IR analyses, that PI networks consisting of perylene and triazine units were formed.

Powder X-ray diffraction (XRD) measurements of **PI-1** and **PI-2** showed two broad halos centered around 10 and 27°, respectively (**Figure 6**, **Table S1**), as commonly observed for POPs. Several sharp reflexes were superimposed on these broad halos, with comparable reflex positions for **PI-1** and **PI-2** (however with higher intensity reflections for **PI-1**). The sets of characteristic reflexes from the starting materials could not be identified in the products. However, the reflection at 27.6° for both **PI-1** (well-defined) and **PI-2** is indicative of π-stacking interactions (d = 0.32 nm), as commonly found for perylene-based materials, including the starting PTCDA here.[28] The slow addition of melamine dissolved in DMSO during the synthesis of **PI-1** favored ordered domains in the product **PI-1** (and thus yielding more well-defined scattering from π-stacks). In the absence of DMSO (**PI-2**), less order is observed, providing the first indications that DMSO plays a role in the structure-formation and growth processes. This observation was further reinforced when analysis of the porosity of the materials was performed (see below). After pyrolysis, the derived amorphous carbon materials showed only two broad halos, centered at 2θ = 25.2 and 43.9°, typical for the 002 and 101 reflections, respectively, of turbostratic nitrogen-containing carbons.[29] No sharp reflection were found corresponding to Zn-related salts, which is in accordance with the results from SAED and elemental analyses reflecting the very low residual content.

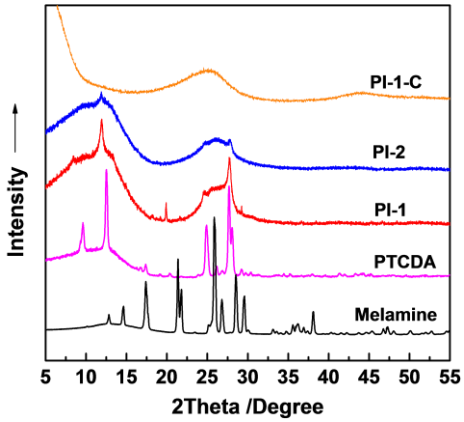

Figure 6 XRD patterns of melamine, PTCDA, **PI-1**, **PI-2** and **PI-1-C**.

We further investigated the chemical composition of the as-synthesized PIs and derived carbons by using X-ray photoelectron spectroscopy (XPS). The XPS survey scans of **PI-1**, **PI-2**, **PI-1-C** and **PI-2-C** clearly showed the presence of C, N, and O as well as Zn (**Figure S8**). Additionally, the spectrum of PI networks synthesized with DMSO (**PI-1**) displayed weak peaks at 228.08 and 164.08 eV due to the sulfur residues. With only the C, N and O atoms taken into account, the relative composition contents of C atoms furthermore increased after the PIs were carbonized, whilst those of N and O decreased (**Table S2**). The C1s core-level XPS spectra of both **PI-1** and **PI-2** showed three peaks: ~288.4 (peak I: originating from the carbonyl groups), ~285.7 (peak II: originating from the triazine units) and ~284.9 eV (peak III: aromatic benzene type units)[30] (**Figure 7**). The N1s core level showed two peaks at ~400.5 (peak I: imide moieties) and ~398.5 eV (peak II: triazine units)[30,31] (**Figure 8**). Oxygen O1s peak deconvolution revealed two peaks at ~532.8 (peak I: carbonyl groups) and ~531.3 eV (peak II: quinone groups)[32] (**Figure 9**). The similarity of the XPS spectra (apart from very weak sulfur residues in **PI-1**) implies that addition of DMSO co-solvent did not change the chemical structure of PI networks.

Theoretically, only three units (1,3,5-triazine, imide and perylene) make up the PI networks. Upon carbonization, these units either remain and/or were transformed to pyridine- and graphite-type carbons. The relative areas of all the peaks dramatically changed and their binding energies slightly decreased, indicating substantial changes of the chemical structure. After carbonization, the area ratios of peak II/peak I of N1s ($R^{II/I}$) observed in **PI-1** and **PI-2** increased from 0.82 to 1.07 and 0.76 to 0.82 (**Table S3**), whilst those values of O1s ($R^{II/I}$) decreased from 1.28 to 0.64 and 1.42 to 1.07, respectively. The results furthermore indicated that some of the imide nitrogen content was either lost to the gas phase or was transferred to pyridine-type nitrogens during the pyrolysis. This is well in accordance with the area ratio changes that were observed for C1s peaks, in which the relative concentrations of oxygen-connected carbons ($R^{I/III}$) decreased (e.g., **PI-1** and **PI-1-C**: 0.56 *vs.* 0.46) while those of pyridine-type carbons ($R^{II/III}$) increased (e.g., **PI-1** and **PI-1-C**: 1.32 *vs.* 2.07). The XPS results indicated that the obtained carbons consist mainly of remained PI segments, pyridinic and triazine structures as well as extended aromatic carbon sheets.

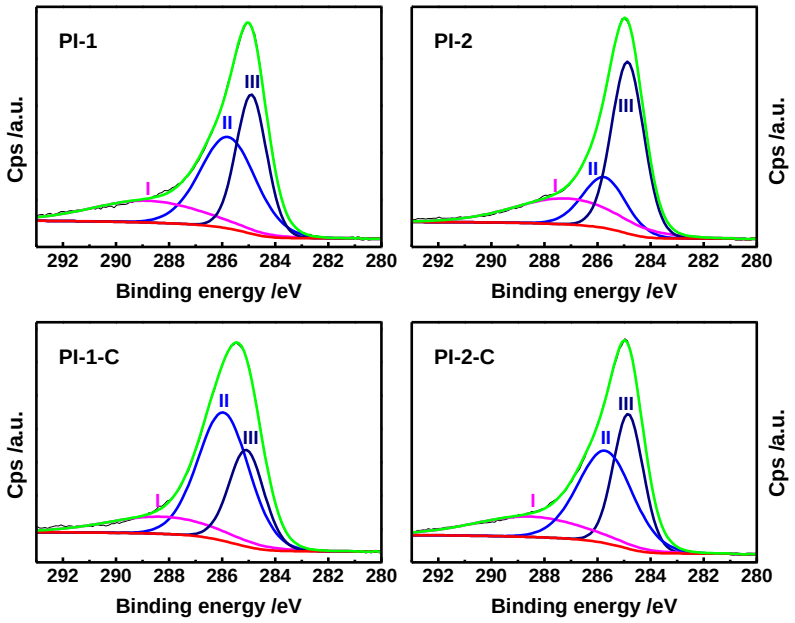

Figure 7 C1s core-level XPS spectra of PIs and derived carbons.

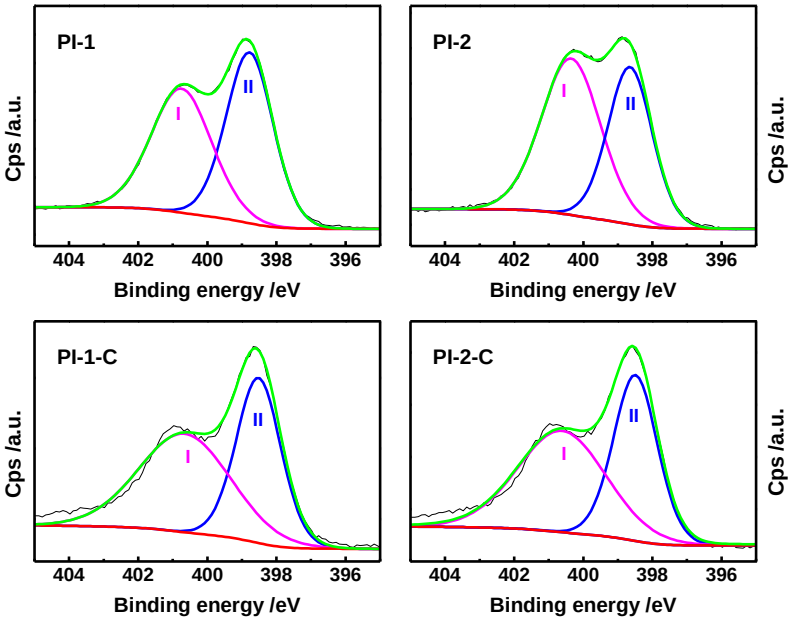

Figure 8 N1s core-level XPS spectra of PIs and derived carbons.

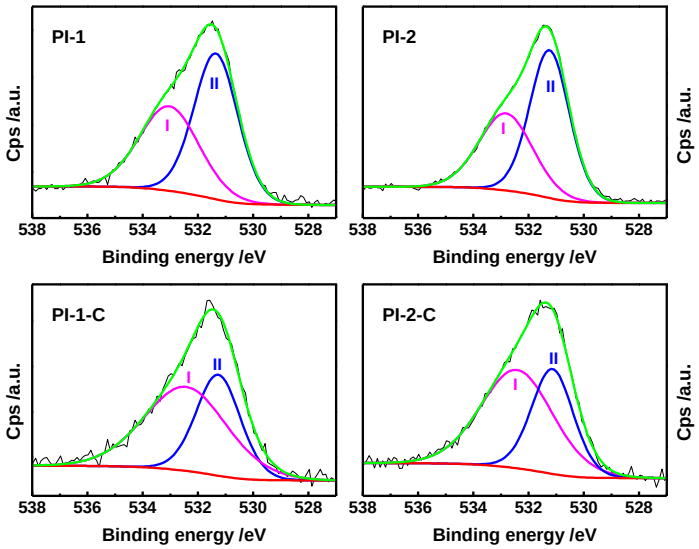

Figure 9 O1s core-level XPS spectra of PIs and derived carbons.

Fluorescence and sensing properties. The THF dispersions (0.5 g L^{-1}) of **PI-1** and **PI-2** displayed strong yellow-green fluorescence and stand in contrast to the weak red fluorescence of PTCDA (**Figure 10**, left panels) recorded at the same concentration. Compared with the PTCDA monomer, the fluorescence spectra (**Figure 10**, right panels) showed hypsochromic shifts (530 *vs.* 522 nm) of the maximum emission bands for PI, with the Stoke's shift decreased by 21 nm (23 *vs.* 44 nm) and the fluorescence intensities increased 7 times. Based on the fluorescence emission (**Figure 10**, right panels) and UV-Vis/NIR absorbance (**Figure S9**) of the THF dispersions, the fluorescence quantum yields of the PTCDA and PIs can be further calculated and compared.[33] It was found that the fluorescence quantum yields were increased 21 times (0.85 *vs.* 0.04) for our PI materials. The reduced π–π stacking of PIs relative to PTCDA would likely hinder self-quenching that arises from strong interactions among the perylene molecules and hence explains the amplified fluorescence that was observed.

We further investigated the fluorescence stability against external stimuli. Upon addition of different heavy metal ions (1 mmol L^{-1}) including Cu^{2+}, Fe^{2+}, Co^{2+}, Mn^{2+}, Pb^{2+}, Fe^{3+}, and Al^{3+} into the **PI-1** dispersion, we observed 15-20% decreases in fluorescence intensities for most of the metal ions (**Figure S10**). Obvious fluorescence quenching (56%) was however found for Fe^{3+}. Among these ions, Fe^{3+} is the most electron-deficient ion and possesses the highest electron-affinity. Fe^{3+} could easily form a complex with electron-rich units[34] such as perylene leading to typical fluorescence quenching. The sensitivity towards Fe^{3+} was however quite low (since high

concentration, 1 mmol L^{-1}, of sensing target was used). As the PI networks are not soluble, the perylene units can be only accessed by the metal ions either *via* the fairly small micropores (see details in below) or through interactions with the particle outer surface. Diffusion into the small pores could be hindered, thus making application of the materials less likely. Considering their low band gap energies (~ 0.9 eV), electron-donor characteristics and stable fluorescence, the PI networks may however be useful in some target applications that require organic conjugated materials with stable and robust optical properties.

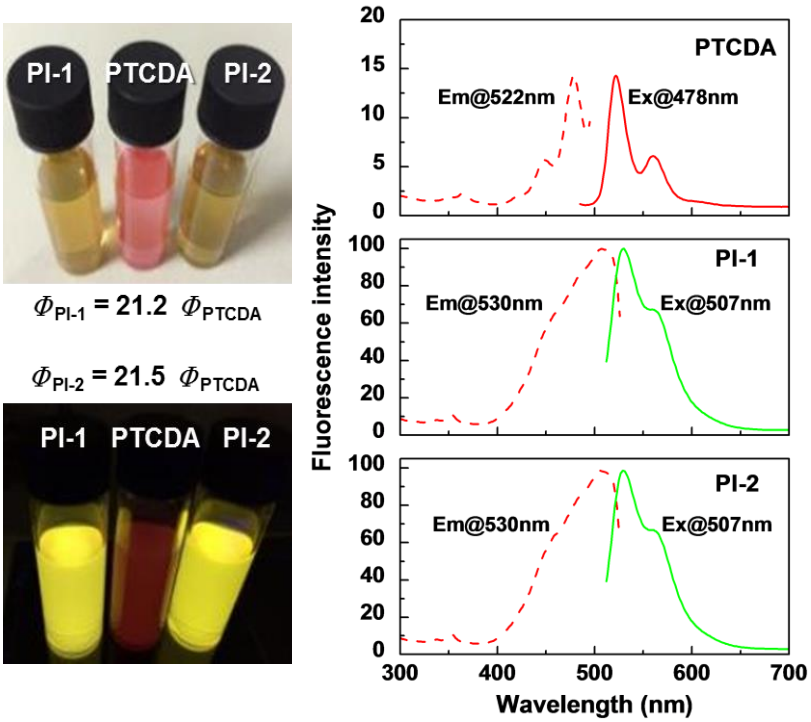

Figure 10 (Left panels) **PI-1**, **PI-2**, and PTCDA as THF dispersions (0.5 g L^{-1}) excited by sunlight and 365 nm UV-vis light; (right panels) excitation and emission fluorescence spectra of corresponding samples.

Surface area and porosities. Initial porosity analyses of **PI-1**, **PI-2** and **PI-1-C** were conducted using N_2 adsorption/desorption experiments at 77.4 K (see **Figure S11** and **Table 1**). No significant uptake of N_2 into micropores was observed for these materials. Some uptake was observed at higher relative pressure, indicative of the presence of interparticle void spaces or macropores.

Table 1 Porosity parameters and CO_2 sorption properties of the PIs and derived carbon.

Materials	S_{BET}[a]	$S_{\mu\text{-pore}}$ [b]	$V_{micropore}$[b]	CO_2 uptake at 1 bar (mmolg^{-1} and wt%)	
	(m^2 g^{-1})	(m^2 g^{-1})	(cm^3 g^{-1})	273 K	303 K
PI-1	19	148	0.043	0.69 (3.0 wt%)	0.44 (1.9 wt%)
PI-2	16	n.d.	n.d.	0.21 (0.9 wt%)	n.d.
PI-opt	n.d.	283	0.084	1.31 (5.8 wt%)	n.d.
PI-1-C	13	483	0.125	2.35 (10.3 wt%)	1.76 (7.7 wt%)
PI-opt-C	181	710	0.177	3.40 (15.0 wt%)	2.42 (10.6 wt%)

[a] Surface area calculated from nitrogen adsorption isotherms using the BET equation; [b] from GCMC analysis of the CO_2 adsorption data at 273 K.; n.d.: not determined.

This finding is in accordance with electron microscopy data (**Figures 1-3** and **Figure S2**). Low specific BET surface areas of < 20 m^2 g^{-1} were calculated from the adsorption data, also in line with the presence of an outer surface only. It is well-known that very narrow and small micropores are hard to assess by cryogenic N_2 adsorption/desorption. However, CO_2 adsorption at 273.15 K provides a feasible option[35] for such materials where microporosity is expected but hard to assess; we hence analyzed the CO_2 adsorption characteristics.

CO_2 adsorption/desorption was initially measured at 273.15 K for analytical purposes. **Figure 11** shows the CO_2 adsorption/desorption isotherms of **PI-1** and **PI-2** along with other materials (e.g. derived carbons, discussed later in the manuscript). It should be noted that the materials showed a weak adsorption/desorption hysteresis. **PI-1** does show a moderate CO_2 uptake of ~ 0.7 mmol g^{-1} (3 wt%). This value is comparable to results found for previously synthesized BPDA-based PIs.[15] Pore size distribution analysis (using the adsorption branch, **Figure 12**) by commercialized methods (Grand-Canonical Monte-Carlo, GCMC) indicated a micropore surface area of 148 m^2 g^{-1} and a narrow pore size distribution with a maximum at ~2.5 Å pore radius. In contrast, **PI-2** synthesized in absence of DMSO did not show any significant CO_2 uptake (~ 0.2 mmol g^{-1}, 0.9 wt%), and was hence not further analyzed.

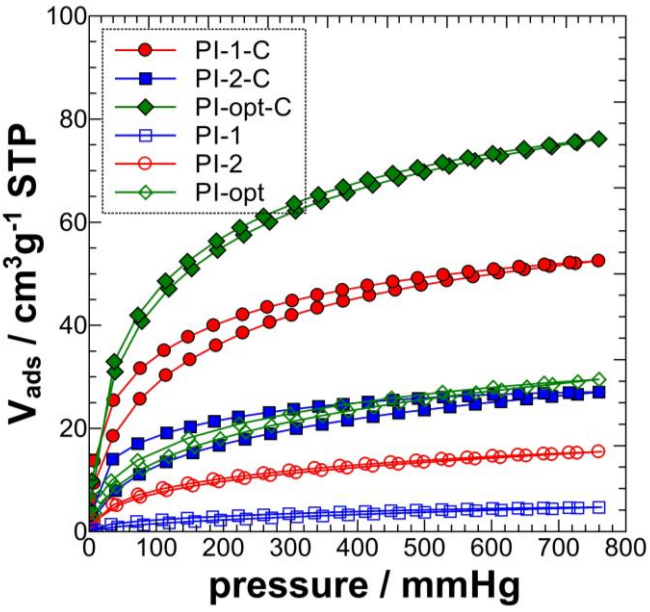

Figure 11 CO_2 adsorption/desorption isotherms of **PI** networks and derived carbons at 273.15 K.

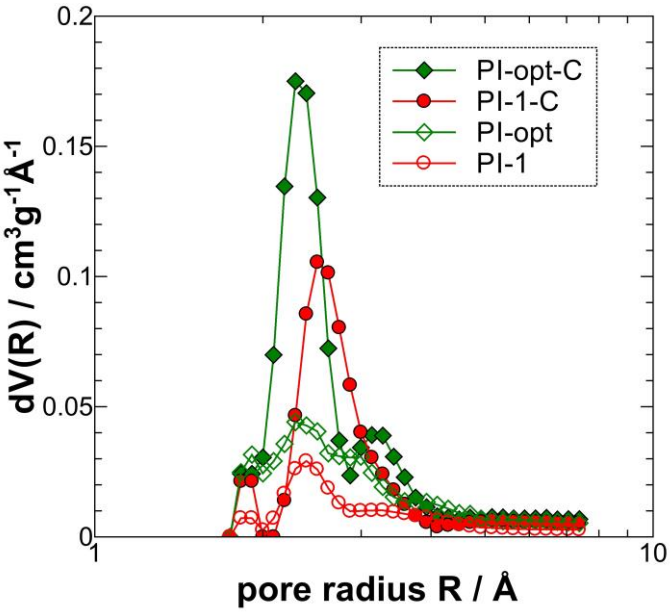

Figure 12 Pore size distribution (PSD) of **PI-1**, **PI-opt** and the derived carbons (**PI-1-C** and **PI-opt-C**) as determined from GCMC-analysis of CO_2 adsorption isotherms at 273.15 K.

The porosity difference between **PI-1** and **PI-2** triggered the question whether DMSO acts as an indirect template. In order to test these hypotheses, a series of PI networks were prepared using various amounts of DMSO during synthesis. Melamine was dissolved in DMSO at concentrations of 30, 6, 3.3, and 2.5 g L^{-1}, and those solutions were used to prepare different PI networks for comparison. According to the CO_2 adsorption/desorption isotherms of the series (measured at

273.15 K, **Figure S12**), the obtained PIs showed an increasing porosity with increasing DMSO content up to a maximum level of a CO_2 uptake of 5.9 wt% at 273.15 K and 1 bar (**Figure 13**). This maximum was observed at a melamine concentration of 6 g L^{-1} corresponding to a DMSO content of 25 mL within the reaction mixture. The maximum CO_2 uptake is ~ 6 times higher than the value obtained by **PI-2** synthesized without DMSO (5.9 *vs.* 0.9 wt%).

Interestingly, the porosity showed a strong decrease upon further increasing the DMSO content within the mixture (**Figure S13**). We suspect that the DMSO content (which makes up half of the total solvent for these materials, e.g. for the 2.5 g L^{-1} investigation) is too high to allow for efficient crosslinking. This in turn could lead to a lowered porosity at such high dilutions, as the connection between high conversion and high porosity is well accepted.[22,23] In contrast, high reactant concentrations ($c_{melamine} \geq 30$ g L^{-1}) led to gelation within the first few minutes of the polymerization. This could again hinder efficient crosslinking and full conversion. Polymer precipitates easily formed at moderate concentrations (3.3 to 15 g L^{-1}), leading to permanent micropores. In summary, a strong dependence of the observable porosity within the **PI-1** type networks on the DMSO content is obvious. Whether this effect is indeed templating or whether it could be explained by the changed phase separation conditions can however not be answered in full detail at this stage, but presents a facile approach to tuning porosity and related properties.

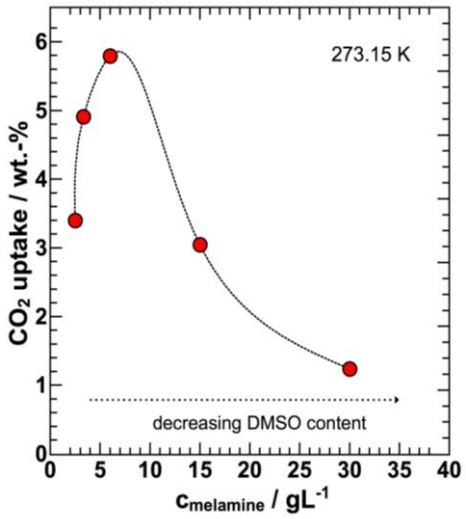

Figure 13 CO_2 uptake (at 273.15 K and 1 bar) of **PI-1** type networks synthesized using various concentrations of melamine in DMSO (and hence different DMSO content within the reaction mixtures).

The PI synthesized with the optimal DMSO content as identified (**PI-opt**), $c_{melamine}$ = 6 g L^{-1} was also carbonized at 800 °C under argon, producing derived carbon material **PI-opt-C** for comparison to the carbons obtained from pyrolysis of **PI-1** and **PI-2** (**PI-1-C** and **PI-2-C)**. **PI-1-C** shows significant microporosity when analyzed by CO_2 adsorption with micropore surface areas up to 483 $m^2 g^{-1}$ and a very narrow pore size distribution with pore sizes predominantly below 0.6 nm (see **Table 1** and **Figures 11**,**12**). Contrary, **PI-2-C** does show only slightly increased porosity ($S_{\mu\text{-pore}}$ = ~ 260 $m^2 g^{-1}$) compared to the parent **PI-2**. Further analysis did hence not include **PI-2-C**. Compared to **PI-1-C**, **PI-opt-C** has a higher much higher porosity as evidenced from CO_2 adsorption ($S_{\mu\text{-pore}}$ = ~ 710 $m^2 g^{-1}$). Interestingly, cryogenic N_2 adsorption also evidenced some microporosity (S_{BET} ~ 181 $m^2 g^{-1}$), which is in contrast to the other carbon materials addressed herein. Still, the N_2 adsorption seems to underestimate the microporosity, which is a common problem for materials with very small pore sizes. **Table 1** summarizes the porosity data, **Figure S14** and **Table S5** provides a detailed comparison with other microporous materials. The **PI-opt-C** showed the highest CO_2 uptake of 3.4 mmol g^{-1} (15 wt%) at 273 K and 1 bar, which is highly comparable with some state-of-the-art carbon materials such as carbon molecular sieves (CMS), activated carbons, and other nitrogen-containing carbons,[36] and considerably better than most reported results for PIs as well as other recently reported porous materials[37] with significantly higher BET surface areas (see **Figure S14** for a graphical comparison of our and related materials). **PI-1-C** and **PI-2-C** showed only 2.35 mmol g^{-1} (10.3 wt%) and 1.22 mmol g^{-1} (5.4 wt%) of CO_2 uptake under the same conditions, respectively. Based on the data obtained from CO_2 adsorption, it can be stated that pyrolysis led to increased porosity compared with the parent PI in all cases, and the structure-templating role of DMSO was also reflected in the CO_2 uptake, and thus also applicable to carbons. A high porosity of the initial PI network is however required for a highly porous carbon.

It appears that the main fraction of pores of **PI-opt-C** is of even smaller size than those of **PI-1-C**. Such very narrow pore size distributions can indeed be of interest for gas separation processes by a combination of kinetic separation and chemical enhancement provided by surface functionalities.[38] Hence, the gas adsorption characteristics in terms of gas selectivity of the two carbons and one parent PI network were analyzed in greater detail and are discussed within the next section.

CO_2 adsorption and selectivity at ambient temperature (303K). To predict the potential of the materials for CO_2/N_2 separation, it is not only necessary to measure single gas uptake capacities, but also to estimate gas selectivity. To do so, we make use of the ideal adsorbed solution theory (IAST).[39] Selectivity calculations are based on the respective adsorption isotherms that were measured at 303 K, i.e. near ambient temperatures that are relevant for real applications (**Table S4**). **PI-1** showed a low CO_2 uptake of 0.44 mmol g^{-1} (1.9 wt%) at 303 K and 1 bar. The N_2 uptake of **PI-1** under same conditions was also low at 0.0166 mmol g^{-1} (0.046 wt%), resulting in an equilibrium selectivity of 26.5. We also analyzed the IAST selectivity for **PI-1**, which gave extremely high selectivities of $\alpha(CO_2/N_2) > 1000$ at a gas composition of 15 v/v% CO_2 (balance made up with N_2, see **Figure S15** and **Figure S16**, **ESI**). Such high values have also been reported for other microporous PIs,[40] which had however a slightly higher total CO_2 uptake. However, although the selectivity calculated here is high, the overall predicted uptake of CO_2 from the gas mixture is only 0.18 mmol g^{-1} at 303 K and 1 bar, which is too low for any reasonable application.

The favorable pore size distributions of **PI-1-C** and **PI-opt-C** (**Figure 12**), which are comparable to those of corresponding parent PI networks, indicated promise for CO_2 separation. **PI-1-C** and **PI-opt-C** showed good CO_2 uptake of 1.76 mmol g^{-1} (7.7 wt%) and 2.42 mmol g^{-1} (10.7 wt%) at 303 K and 1 bar (**Figure S17**), respectively. The N_2 uptakes of **PI-1-C** and **PI-opt-C** under the same conditions were 0.12 mmol g^{-1} (0.33 wt%) and 0.19 mmol g^{-1} (0.53 wt%), resulting in a moderate equilibrium selectivity of 14.7 and 12.7, respectively. We also calculated the IAST selectivity and predicted adsorption isotherms of the carbons based on the fitted adsorption branches of the isotherms (**Figures S18,19**). For **PI-1-C**, a high IAST CO_2 over N_2 selectivity, α (CO_2/N_2) ~ 85 was found at 303 K and 1 bar, at a gas composition of 15 v/v% CO_2 (balance made up with N_2, see **Figure 14**). The predicted adsorption capacity of CO_2 from the gas mixture is 0.8 mmol g^{-1} (3.4 wt%), which is approximately a factor of two lower compared to the capacity with respect to the pure gas. For **PI-opt-C**, the predicted selectivity and adsorption capacity of CO_2 over N_2 (15 : 85) could be improved to 240 and 1.18 mmol g^{-1}, respectively. Such values are very acceptable given the rather high selectivity, and indeed make such materials promising for gas separation applications, especially as the working capacity exceeds that of benchmark and activated carbons (BPL and MAXSORB), which were reported to have working capacities of 0.4-0.5 mmol g^{-1} at 1 atm.[41]

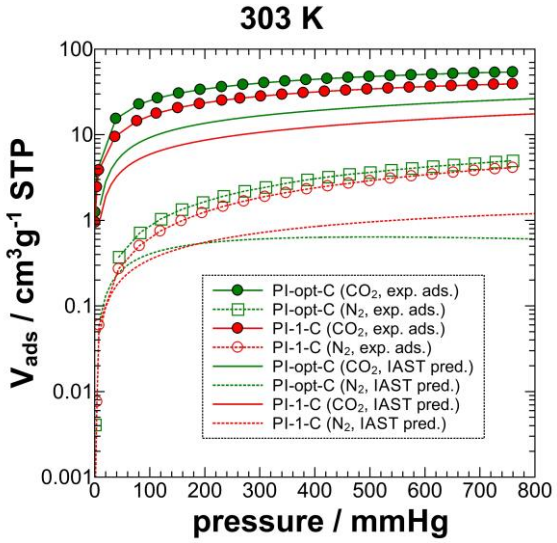

Figure 14 CO_2 and N_2 experimental adsorption isotherms (single gas) of **PI-1-C** and **PI-opt-C** at 303 K (symbol+line) together with predicted adsorption isotherms (line only) from a 0.15/0.85 v/v gas mixture of CO_2 and N_2 at 303 K (based on IAST methodology).

The high selectivity can, in our opinion, be mainly attributed to the presence of very narrow micropores, which are known to adsorb CO_2 strongly at ambient pressures.[40,42,43] The high selectivity might additionally benefit from a moderately high estimated isosteric heat of adsorption, which is probably due to a combination of the very narrow pores, which lead to increased bond strength due to overlap of attractive potentials from *both* pore walls, and the chemical functionalities that were evidenced by XPS. The heat of adsorption q_{st} was found to vary from 38 kJ mol^{-1} at zero loading to 25 kJ mol^{-1} at 2 mmol g^{-1} CO_2 loading (**PI-1-C**). The variation of the heat of adsorption with loading is also reflected in the fit quality. The CO_2 adsorption branch could only be fitted using a dual-site Langmuir approach, indicating the energetic and morphological heterogeneity of the surface. It is noteworthy that the CO_2 and N_2 adsorption data of **PI-1-C** and **PI-opt-C** at 303 K showed some hysteresis, which was typically observed for ultrasmall pore sizes and kinetic issues of microporous materials.[6]

We also analyzed the IAST selectivity of **PI-I-C** based on the desorption branches of CO_2 and N_2 isotherms (see **Figure S18**, **ESI**) and found much higher selectivity of ~ 500 at 1 bar and 303 K at a comparable CO_2 uptake from the mixture (see **Table S5** for a detailed comparison of the values obtained here with other published data). The difference in values (when compared to data from the adsorption branches above) might be related to the different slopes at high pressure and

predictions about total uptake obtained from the fit parameters of the Langmuir models. At this stage, we can nevertheless summarize that carbon materials of very good CO_2 sorption capacity were prepared. First predictions concerning the selectivity (demonstrated for the CO_2/N_2 gas pair) indicate excellent selectivity and make these materials promising for real gas separation applications.

Conclusions

We have successfully synthesized novel microporous polyimide (PI) networks comprised of perylene and triazine units *via* a condensation method. The obtained PI networks (in the presence or absence of DMSO, a high boiling point solvent and indirect template) showed good thermal stability, and could be further pyrolyzed to produce microporous carbon materials. Both PIs and derived carbon materials have moderate micropore surface areas (up to 483 and 710 $m^2\ g^{-1}$, respectively) and feature a very sharp and narrow pore size distribution, with uniform ultra-micropores less than 6 Å. The parent PIs feature extremely high selectivity for CO_2 over N_2 (> 1000) with moderate CO_2 capacity (5.9 wt%). The derived carbon materials however show significantly higher CO_2 uptakes of up to 15 wt% while maintaining very good CO_2/N_2 adsorption IAST selectivities of α = 240 at 303 K and 1.0 bar. These results show that this novel class of PIs and carbons derived from perylene and triazine units are very competitive candidates for CO_2 capture. With the low band gap energy (~0.9 eV), fluorescence and electron-donor characteristics, parent PI networks are also promising for other target applications such as organic photovoltaics, solar cells and photocatalysis.

Experimental

Materials. Perylene-3,4,9,10-tetracarboxylic dianhydride (PTCDA), melamine, imidazole, $Zn(OAc)_2$, dimethyl sulfoxide (DMSO), dimethylformamide (DMF), tetrahydrofuran (THF), other solvents with an assay of >97% were purchased from Sigma-Aldrich and used as received.

Synthesis of PI networks. PTCDA (594 mg, 1.5 mmol) was mixed with imidazole (52.5 g) and $Zn(OAc)_2$ (417 mg) and stirred at 200 ^oC under nitrogen atmosphere for 30 min until dissolved. To this mixture melamine (150 mg, 1.2 mmol) dissolved in DMSO (10 mL, i.e., the concentration of melamine in DMSO is 15 g L^{-1})[44] was added dropwise (~3 μL s^{-1}) and stirred at 200 ^oC for 24 h.

The mixture was then reacted at 180 °C for a further 72 h. After this the reaction mixture was cooled to 100 °C and methanol was added. The formed precipitate was collected by filtration, followed by washing with DMF and methanol, and then dried overnight at 100 °C in a vacuum oven to obtain 360 mg of **PI-1** (yield: 54%). *Anal. Calcd.* for $C_{69}H_{30}N_6O_6$: C, 73.76; H, 2.91; N, 8.09; O, 9.24. *Found*: C, 73.46; H, 3.65; N, 9.43; O, n. d. A series of concentrations of melamine in DMSO normally 30, 15, 6, 3.3 and 2.5 g L^{-1}, were used to synthesize PI networks in order to investigate the "template" effect of DMSO in micropore formation. If it is not specifically indicated, **PI-1** mentioned is the PI network synthesized at a concentration of 15 g L^{-1}. **PI-2** was synthesized in the absence of DMSO for comparison. The same reaction procedure as described for the synthesis of **PI-1** provided 315 mg of **PI-2** (yield: 47%). *Anal. Calcd.* for $C_{69}H_{30}N_6O_6$: C, 73.76; H, 2.91; N, 8.09; O, 9.24. *Found*: C, 70.11; H, 2.65; N, 8.34; O, n. d.

Synthesis of PI derived carbon materials. **PI-1** powder (320 mg) was heated to 800 °C in argon at a rate of 5 °C/min and then carbonized for 30 min, 215 mg of nitrogen-doped carbon materials (**PI-1-C**) with a char yield of 67.9% were obtained. *Anal. Found.* for **PI-1-C**: C, 83.31%; H, 0.78%; N, 3.01%; S, 0.08%.

Characterization and measurements. Elemental analyses (C/H/N/S) were carried out using a Euro Vector EuroEA3000 Elemental Analyzer. A weighed sample was decomposed in Aqua Regia and then diluted to an accurate volume. Then the zinc content was determined on a GBC Avanta Sigma atomic absorption spectrophotometer operating in the Graphite Furnace mode against known standards. Solid-state and dispersion-state ultraviolet visible near infrared (UV-Vis/NIR) spectra of samples as powders and THF dispersions were acquired on a Shimadzu UV-2600 Spectrometer, respectively. Fourier transform infrared (FT-IR) spectra were taken on a Perkin Elmer Spectrum 100 spectrometer. Fluorescence spectra of PTCDA, **PI-1**, and **PI-2** as THF dispersions were acquired on a JASCO FP-6500 spectrofluorometer. Powder X-ray diffraction (XRD) patterns were obtained on a Bruker D8 Advance diffractometer (40 kV, 30 Ma) using Cu Kα radiation (2θ = 5–55°). Solid-state ^{13}C CP/MAS nuclear magnetic resonance (^{13}C CP/MAS NMR) spectra were recorded at Solid state NMR Service, Durham University on a Varian VNMRS-600 spectrometer using a spin-rate of 6800 Hz. X-ray photoelectron spectra were obtained at the National EPSRC XPS User's Service (NEXUS) at Newcastle University using a K-Alpha (Thermo Scientific, East Grinstead, UK) facility (X-ray energy: 1486.6 eV; Spot size:

400 × 800 microns; Pass energy: Surveys 200 eV, High resolution regions 40 eV; Dwell time: Surveys 10 ms, high resolution regions 100 ms; Charge neutralisation: ON). The obtained spectra were further analyzed using a CasaXPS software. Thermal gravimetric analysis (TGA) was carried out on a TGA Q500 apparatus in nitrogen atmosphere (flow rate 30 mL min^{-1}) in the temperature range 30–1000 ^{o}C (heating rate 10 ^{o}C min^{-1}). Scanning electron microscope (SEM) images and Energy dispersive X-ray (EDX) spectra were obtained on a JEO 5600LV SEM microscope equipped with an EDX spectrometer. High-resolution transmission electron microscope (TEM) images and selected area electron diffraction (SAED) patterns were obtained on a JEOL 2010 TEM microscope. Nitrogen adsorption/desorption measurements at 77.4 K were performed after degassing the samples under high vaccum at 70 °C for at least 20 hours using a Quantachrome Quadrasorb SI-MP machine. CO_2 and N_2 adsorption/desorption isotherms at 273 and 303 K were conducted on a Quantachrome Autosorb-1MP instrument after prior degassing under high vacuum (turbomolecular pump) and 70°C. The specific surface areas were calculated by applying the Brunauer-Emmett-Teller (BET) model to adsorption branches of the isotherms (N_2 at 77.4 K) the QuadraWin 5.05 software package. Analysis of the isotherms by commercialized Grand-canonical Monte-Carlo (GCMC) methodology[45] was also done using either the QuadraWin 5.05 or AS1Win package of Quantachrome Instruments.

Fluorescence quantum yield calculation and sensing properties. The relative fluorescence quantum yield (Φ) of the PTCDA and PIs in solution can be calculated using equation (1).[33]

$$\Phi = \frac{{n_s}^2 A_r I_{s-r}}{{n_r}^2 A_s I_{r-s}} \qquad (1)$$

Here A_r and A_s are the absorbances of the sample and reference solutions at the excitation wavelength; I_s and I_r are the corresponding emission integration areas; and Φ_s and Φ_r are quantum efficiencies of the sample and reference compound; n_s and n_r are refractive indices of the sample and standard solutions. In this study, Rhodamine 101 and THF were used as the fluorescent reference and solvent. The fluorescence quantum yields of PTCDA, **PI-1** and **PI-2** are calculated to be 0.04, 0.85 and 0.86, respectively. The sensing properties were studied based on the standard fluorescence quenching protocol. Fluorescence quenching was performed by sequentially adding 0.2 mL of different analytes including Cu^{2+}, Fe^{2+}, Co^{2+}, Mn^{2+}, Pb^{2+}, Fe^{3+} and Al^{3+} to 3 mL of a **PI-1** THF dispersion (0.5 g L^{-1}).

***IAST Calculations*.** Selectivity was calculated using the common IAST equation (2).[39]

$$\alpha = \frac{x_{CO_2}/x_{N_2}}{y_{CO_2}/y_{N_2}} \qquad (2)$$

Here α is the selectivity, *x* the adsorbed amount and *y* represents the gas phase composition. x_{CO2} was determined using a Newton-Raphson method implemented within a *MatLab*® (*R2011a*) script or an *octave* (open source software) script, these scripts are available for download at: http://f-n.hszg.de/fakultaet/hochschullehrerinnen/jens-weber/jens-weber/vermischtesdownloads.html or upon request *via* e-mail. The amount adsorbed from the mixed-gas phase was also determined following the known protocols based on Ref. 41 using the respective fit parameters as basis for the analytical description of the single-gas adsorption isotherms. The gas phase composition was set 15 vol.-% CO_2 and 85 vol.-% N_2, *i.e.* $y_{CO2} = 0.15$ and $y_{N2} = 0.85$.

Acknowledgements

We are grateful to the European Commission Marie Curie International Incoming Fellowship (FP7-PEOPLE-2012-IIF TANOGAPPs No. 326385) for generous support of this project and Mr. Jonathan A. Jones (University of Bristol) for TEM measurements. Jessica Brandt (MPIKG) is acknowledged for laboratory assistance and NEXUS NanoLab (Newcastle University) for XPS measurements.

References and Notes

1. a) P. Mohanty, L. D. Kull and K. Landskron, *Nat. Comm.,* 2011, **2**, 1-6; b) S. C. Xiang, Y. B. He, Z. J. Zhang, H. Wu, W. Zhou, R. Krishna and B. L. Chen, *Nat. Comm.,* 2012, **3**, 1-9; c) J.-R. Li, J. M. Yu, W. G. Lu, L.-B. Sun, J. Sculley, P. B. Balbuena and H.-C. Zhou, *Nat. Comm.,* 2013, **4**, 1-8.
2. a) S. W. Yuan, B. Dorney, D. White, S. Kirklin, P. Zapol, L. P. Yu and D.-J. Liu, C*hem. Commun.*, 2010, **46**, 4547-4549; b) R. Dawson, E. Stöckel, J. R. Holst, D. J. Adams and A. I . Cooper, *Energy Environ. Sci.*, 2011, **4**, 4239-4245; c) V. M. Suresh, S. Bonakala, H. S. Atreya, S. Balasubramanian and T. K. Maji, *ACS Appl. Mater. Inter.*, 2014, **6**, 4630-4637.
3. a) P. M. Budd, E. S. Elabas, B. S. Ghanem, S. Makhseed, N. B. McKeown, K. J. Msayib, C. E. Tattershall and D. Wang, *Adv. Mater.*, 2004, **16**, 456-459; b) P. M. Budd, N. B. McKeown and D. Fritsch, *J. Mater. Chem.*, 2005, **15**, 1977-1986; c) N. B. McKeown and P. M. Budd,

Macromolecules, 2010, **43**, 5163-5176; d) R. Short, M. Carta, C. G. Bezzu, D. Fritsch, B. M. Kariuki and N. B. McKeown, *Chem. Commun.*, 2011, **47**, 6822-6824.

4. a) A. P. Côté, A. I. Benin, N. W. Ockwig, M. O'Keeffe, A. J. Matzger and O. M. Yaghi, *Science*, 2005, **310**, 1166-1170; b) H. M. El-Kaderi, J. R. Hunt, J. L. Mendoza-Cortés, A. P. Côté, R. E. Taylor, M. O'Keeffe and O. M. Yaghi, *Science*, 2007, **316**, 268-272; c) H. Furukawa and O. M. Yaghi, *J. Am. Chem. Soc.*, 2009, **131**, 8875-8883; d) S.-Y. Ding, J. Cao, Q. Wang, Y. Zhang, W.-G. Song, C.-Y. Su and W. Wang, *J. Am. Chem. Soc.*, 2011, **133**, 19816-19822; e) J.-T. Yu, Z. Chen, J. Sun, Z.-T. Huang and Q.-Y. Zheng, *J. Mater. Chem.*, 2012, **22**, 5369-5373; f) X. Chen, M. Addicoat, S. Irle, A. Nagai and D. L. Jiang, *J. Am. Chem. Soc.*, 2013, **135**, 546-549.
5. a) P. Kuhn, M. Antonietti and A. Thomas, *Angew. Chem. Intern. Edit.*, 2008, **47**, 3450-3453; b) C. E. Chan-Thaw, A. Villa, P. Katekomol, D. S. Su, A. Thomas and L. Prati, *Nano Lett.*, 2010, **10**, 537-541; c) M. J. Bojdys, J. Jeromenok, A. Thomas and M. Antonietti, *Adv. Mater.*, 2010, **22**, 2202-2205; d) S. J. Ren, M. J. Bojdys, R. Dawson, A. Laybourn, Y. Z. Khimyak, D. J. Adams and A. I. Cooper, *Adv. Mater.*, 2012, **24**, 2357-2361.
6. a) J. Weber and A. Thomas, *J. Am. Chem. Soc.*, 2008, **130**, 6334-6335; b) J.-X. Jiang, A. Trewin, F. B. Su, C. D. Wood, H. J. Niu, J. T. A. Jones, Y. Z. Khimyak and A. I. Cooper, *Macromolecules*, 2009, **42**, 2658-2666; c) L. Chen, Y. Honsho, S. Seki and D. L. Jiang, *J. Am. Chem. Soc.*, 2010, **132**, 6742-6748; d) F. Vilela, K. Zhang and M. Antonietti, *Energy Environ. Sci.*, 2012, **5**, 7819-7832; e) D. B. Xiao, Y. Li, L. L. Liu, B. Wen, Z. J. Gu, C. Zhang and Y. S. Zhao, *Chem. Commun.*, 2012, **48**, 9519-9521; f) Y. H. Xu, A. Nagai and D. L. Jiang, *Chem. Commun.*, 2013, **49**, 1591-1593; g) Y. H. Xu, S. Jin, H. Xu, A. Nagai and D. L. Jiang, *Chem. Soc. Rev.*, 2013, **42**, 8012-8031; h) Y. Z. Liao, J. Weber and C. F. J. Faul, *Chem. Commun.*, 2014, **50**, 8002-8005; i) P. Kuhn, A. Forget, D. Su, A. Thomas and M. Antonietti, *J. Am. Chem. Soc.*, 2008, **130**, 13333-13337.
7. a) C. D. Wood, B. Tan, A. Trewin, H. J. Niu, D. Bradshaw, M. J. Rosseinsky, Y. Z. Khimyak, N. L. Campbell, R. Kirk, E. Stockel and A. I. Cooper, *Chem. Mater.*, 2007, **19**, 2034-2048; b) B. Li, X. Huang, L. Liang and B. Tan, *J. Mater. Chem.*, 2010, **20**, 7444-7450; c) X. Zhu, S. M. Mahurin, S. H. An, C. L. Do-Thanh, C. Tian, Y. K. Li, L. W. Gill, E. W. Hagaman, Z. J. Bian, J.-H. Zhou, J. Hu, H. L. Liu and S. Dai, *Chem. Commun.*, 2014, **50**, 7933-7936.

8. W. G. Lu, J. P. Sculley, D. Q. Yuan, R. Krishna, Z. W. Wei and H.-C. Zhou, *Angew. Chem. Intern. Edit.*, 2012, **51**, 7480-7484.
9. B. Kiskan and J. Weber, *ACS Macro Lett.*, 2012, **1**, 37-40.
10. G. Y. Li and Z. G. Wang, *Macromolecules*, 2013, **46**, 3058-3066.
11. a) H. A. Patel, F. Karadas, A. Canlier, J. Park, E. Deniz, Y. S. Jung, M. Atilhan and C. T. Yavuz, *J. Mater. Chem.*, 2012, **22**, 8431-8437; b) H. Lim, M. C. Cha and J. Y. Chang, *Macromol. Chem. Phys.*, 2012, **213**, 1385-1390.
12. R. Palkovits, M. Antonietti, P. Kuhn, A. Thomas and F. Schüth, *Angew. Chem. Intern. Edit.*, 2009, **48**, 6906-6912.
13. S. Chu, Y. Wang, Y. Guo, P. Zhou, H. Yu, L. L. Luo, F. Kong and Z. G. Zou, *J. Mater. Chem.*, 2012, **22**, 15519-15521.
14. J. Weber, M. Antonietti and A. Thomas, *Macromolecules*, 2008, **41**, 2880-2885.
15. Y. L. Luo, B. Y. Li, L. Y. Liang and B. E. Tan, *Chem. Commun.*, 2011, **47**, 7704-7706.
16. S. Chu, Y. Wang, Y. Guo, J. Y. Feng, C. C. Wang, W. J. Luo, X. X. Fan and Z. G. Zou, *ACS Catal.*, 2013, **3**, 912-919.
17. J.-D. Xiao, L.-G. Qiu, Y.-P. Yuan, X. Jiang, A.-J. Xie and Y.-H. Shen, *Inorg. Chem. Commun.*, 2013, **29**, 128-130.
18. M. R. Liebl and J. Senker, *Chem. Mater.*, 2013, **25**, 970-980.
19. K. V. Rao, R. Haldar, C. Kulkarni, T. K. Maji and S. J. George, *Chem. Mater.*, 2012, **24**, 969-971.
20. B. S. Ghanem, R. Swaidan, E. Litwiller and I. Pinnau, *Adv. Mater.*, 2014, **26**, 3688-3692.
21. O. K. Farha, A. M. Spokoyny, B. G. Hauser, Y.-S. Bae, S. E. Brown, R. Q. Snurr, C. A. Mirkin and J. T. Hupp, *Chem. Mater.*, 2009, **21**, 3033-3035.
22. P. Pandey, A. P. Katsoulidis, I. Eryazici, Y. Y. Wu, M. G. Kanatzidis and S. T. Nguyen, *Chem. Mater.*, 2010, **22**, 4974-4979.
23. R. Dawson, A. Laybourn, Y. Z. Khimyak, D. J. Adams and A. I. Cooper, *Macromolecules*, 2010, **43**, 8524-8530.
24. J. Germain, F. Svec and J. M. J. Fréchet, *Chem. Mater.*, 2008, **20**, 7069-7076.
25. a) H. Kaiser, J. Lindner and H. Langhals, *Chem. Ber.*, 1991, **124**, 529-535; b) C. D. Schmidt, C. Böttcher and A. Hirsch, *Eur. J. Org. Chem.*, 2007, **33**, 5497-5505.

26. a) L. Chen, Y. Yang and D. L. Jiang, *J. Am. Chem. Soc.*, 2010, **132**, 9138-9143; b) Y. Kou, Y. H. Xu, Z. Q. Guo and D. L. Jiang, *Angew. Chem.* 2011, **123**, 8912-8916.
27. M. G. Schwab, B. Fassbender, H. W. Spiess, A. Thomas, X. L. Feng and K. Mullen, *J. Am. Chem. Soc.*, 2009, **131**, 7216-7217.
28. S. R. Forrest, M. L. Kaplan and P. H. Schmidt, *J. Appl. Phys.*, 1984, **55**, 1492-1507.
29. a) Z. Q. Li, C. J. Lu, Z. P. Xia, Y. Zhou and Z. Luo, *Carbon*, 2007, **45**, 1686-1695; b) Y. Z. Liao, X.-G. Li and R. B. Kaner, *ACS Nano*, 2010, **4**, 5193-5202.
30. H. Konno, T. Nakahashi and M. Inagaki, *Carbon*, 1997, **35**, 669-674.
31. V. N. Khabashesku, J. L. Zimmerman and J. L. Margrave, *Chem. Mater.*, 2000, **12**, 3264-3270.
32. a) U. B. Nasini, V. G. Bairi, S. K. Ramasahayam, S. E. Bourdo, T. Viswanathan and A. U. Shaikh, *J. Power Sources*, 2014, **250**, 257-265; b) T. Le, Y. Yang, Z. H. Huang and F. Y. Kang, *J. Power Sources*, 2015, **278**, 683-692.
33. a) Y. Pang, J. Li and T. J. Barton, *J. Mater. Chem.*, 1998, **8**, 1687-1690; b) Y. Z. Liao, V. Strong, Y. Wang, X.-G. Li, X. Wang and R. B. Kaner, *Adv. Funct. Mater.*, 2012, **22**, 726-735.
34. a) X.-G. Li, Y. Z. Liao, M.-R. Huang, V. Strong and R. B. Kaner, *Chem. Sci.*, **4**, 1970-1978; b) Y. Z. Liao, S. S. Cai, S. J. Huang, X. Wang and C. F. J. Faul, *Macromol. Rapid Commun.*, 2014, **35**, 1833-1839.
35. D. Lozano-Castelló, D. Cazorla-Amorós and A. Linares-Solano, *Carbon*, 2004, **42**, 1233-1242.
36. a) A. Wahby, J. M. Ramos-Fernández., M. Martínez-Escandell., A. Sepúlveda-Escribano, J. Silvestre-Albero and F. Rodríguez-Reinoso, *ChemSusChem*, 2010, **3**, 974-981; b) G. P. Hao, W. C. Li, D. Qian and A. H. Liu, *Adv. Mater.*, 2010, **22**, 7, 853-857; c) C. Pevida, T. C. Drage and C. E. Snape, *Carbon*, 2008, **46**, 1464-1474; d) E. S. Kikkinides, R. T. Yang and S. H. Cho, *Ind. Eng. Chem. Res.*, 1993, **32**, 2714-2720; e) R. V. Siriwardane, M. S. Shen, E. P. Fisher and J. A. Poston, *Energy Fuels*, 2001, **15**, 279-284; f) J. Wei, D. D. Zhou, Z. K. Sun, Y. H. Deng, Y. Y. Xia and D. Y. Zhao, *Adv. Funct. Mater.*, 2013, **23**, 2322-2328.
37. M. M. Wan, H. Y. Zhu, Y. Y. Li, J. Ma, S. Liu and J. H. Zhu, *ACS Appl. Mater. Inter.*, 2014, **6**, 12947-12955.
38. N. P. Stadie, M. Murialdo, C. C. Ahn and B. Fultz, *J. Am. Chem. Soc.*, 2013, **135**, 990-993.

39. A. L. Myers and J. M. Prausnitz, *AIChE J.*, 1965, **11**, 121-127.

40. M. M. Unterlass, F. Emmerling, M. Antonietti and J. Weber. *Chem. Commun.*, 2014, **50**, 430-432.

41. D. M. D'Alessandro, B. Smit and J. R. Long, *Angew. Chem. Int. Ed.*, 2010, **49**, 6058-6082.

42. M. Sevilla, J. B. Parra and A. B. Fuertes, *ACS Appl. Mater. Inter.*, 2013, **5**, 6360-6368.

43. J. M. Bermúdez, P. H. Dominguez, A. Arenillas, J. Cotl, J. Weber and R. Luque, *Materials*, 2013, **6**, 4641-4653.

44. DMSO, imidazole, *m*-cresol and isoquinoline are typical solvents with high boiling point (>180 ^{o}C) used for syntheses of microporous PI networks according to previous studies. DMSO and imidazole are relatively cheaper and lower toxic solvents and able to dissolve melamine well. Solubility tests indicate that other common high boiling point solvents such as *N*-methyl-2-pyrolidone, dimethylformamide are unable to dissolve melamine. Therefore, DMSO and imidazole are the only two solvents used in this study.

45. a) S. Samios, A. K. Stubos, N. K. Kanellopoulos, R. F. Cracknell, G. K. Papadopoulos and D. Nicholson, *Langmuir*, 1997, **13**, 2795-2802; b) A. Vishnyakov, P. I. Ravikovitch and A. V. Neimark, *Langmuir*, 1999, **15**, 8736-8742.

Table of Contents Entry

New microporous polyimide networks were synthesized *via* the condensation of perylene-3,4,9,10-tetracarboxylic dianhydride and melamine using a Lewis acid catalyst zinc acetate/imidazole complex. The polyimide networks are, beside their strong fluorescence, excellent precursors to fabricate nitrogen-doped carbon materials with moderate microporosity (710 m^2 g^{-1}) and uniform narrow pore size distribution (5-6 Å pore width). Realizing high CO_2 uptake (15 wt%) and while simultaneously achieving exceptionally high selectivity (240) at ambient conditions make these materials stand out from other reported investigations into gas sorbents, which usually exhibit a trade-off between CO_2 selectivity and uptake capacity.

Keywords: Microporous polymers, polyimide, perylene, triazine, synthesis

Authors: Yaozu Liao, Jens Weber and Charl F. J. Faul

Title: Fluorescent Microporous Polyimides based on Perylene and Triazine for Highly CO_2-Selective Carbon Materials

TOC figure